

## RESEARCH ARTICLE

Electrospun  $\text{Ca}_3\text{Co}_{4-x}\text{O}_{9+\delta}$  nanofibers and nanoribbons: Microstructure and thermoelectric propertiesKatharina Kruppa<sup>1</sup>  | Itzhak I. Maor<sup>2</sup> | Frank Steinbach<sup>1</sup> | Vadim Beilin<sup>2</sup> | Meirav Mann-Lahav<sup>2</sup> | Mario Wolf<sup>1</sup> | Gideon S. Grader<sup>2,3</sup>  | Armin Feldhoff<sup>1</sup> <sup>1</sup>Institute, of Physical Chemistry and Electrochemistry, Leibniz University Hannover, Hannover, Germany<sup>2</sup>Wolfson Department of Chemical Engineering, Technion—Israel Institute of Technology, Haifa, Israel<sup>3</sup>Grand Technion Energy Program (GTEP), Technion—Israel Institute of Technology, Haifa, Israel

## Correspondence

Gideon S. Grader, Wolfson Department of Chemical Engineering, Technion—Israel Institute of Technology, Haifa 32000, Israel.

Email: [grader@technion.ac.il](mailto:grader@technion.ac.il)

Armin Feldhoff, Institute of Physical Chemistry and Electrochemistry, Leibniz University Hannover, Callinstraße 3A, D-30167 Hannover, Germany.

Email:

[armin.feldhoff@pci.uni-hannover.de](mailto:armin.feldhoff@pci.uni-hannover.de)

## Funding information

Ministry of Science and Culture of Lower Saxony (MWK)

## Abstract

Oxide-based ceramics offer promising thermoelectric (TE) materials for recycling high-temperature waste heat, generated extensively from industrial sources. To further improve the functional performance of TE materials, their power factor should be increased. This can be achieved by nanostructuring and texturing the oxide-based ceramics creating multiple interphases and nanopores, which simultaneously increase the electrical conductivity and the Seebeck coefficient. The aim of this work is to achieve this goal by compacting electrospun nanofibers of calcium cobaltite  $\text{Ca}_3\text{Co}_{4-x}\text{O}_{9+\delta}$ , known to be a promising p-type TE material with good functional properties and thermal stability up to 1200 K in air. For this purpose, polycrystalline  $\text{Ca}_3\text{Co}_{4-x}\text{O}_{9+\delta}$  nanofibers and nanoribbons were fabricated by sol-gel electrospinning and calcination at intermediate temperatures to obtain small primary particle sizes. Bulk ceramics were formed by sintering pressed compacts of calcined nanofibers during TE measurements. The bulk nanofiber sample pre-calcined at 973 K exhibited an improved Seebeck coefficient of  $176.5 \text{ S cm}^{-1}$  and a power factor of  $2.47 \mu\text{W cm}^{-1} \text{ K}^{-2}$  similar to an electrospun nanofiber-derived ceramic compacted by spark plasma sintering.

## KEYWORDS

electron microscopy, electrospinning, microstructure, thermoelectric properties

## 1 | INTRODUCTION

Thermoelectric (TE) energy harvesting is based on the conversion of thermal energy into electric energy in a TE material by thermal induction.<sup>1,2</sup> Optimizing the generators and improving the performance of the TE materials are the two most eminent areas in TE research. This research focuses on improving the performance

of the p-type TE oxide-based  $\text{Ca}_3\text{Co}_{4-x}\text{O}_{9+\delta}$  (CCO) ceramic for high-temperature applications. Compared to conventional materials, such as bismuth telluride ( $\text{Bi}_2\text{Te}_3$ ) and lead chalcogenide  $\text{PbX}$  ( $\text{X} = \text{S}, \text{Se}, \text{or Te}$ ), this ceramic shows relatively low TE performance at ambient temperature but has much higher chemical and thermal stability, making it suitable for high-temperature operations in air. Additionally, CCO is lead-free and consists of more abundant elements than conventional analogs.<sup>3–6</sup>

Katharina Kruppa and Itzhak I. Maor had equal contribution.

This is an open access article under the terms of the [Creative Commons Attribution](https://creativecommons.org/licenses/by/4.0/) License, which permits use, distribution and reproduction in any medium, provided the original work is properly cited.

© 2022 The Authors. *Journal of the American Ceramic Society* published by Wiley Periodicals LLC on behalf of American Ceramic Society.

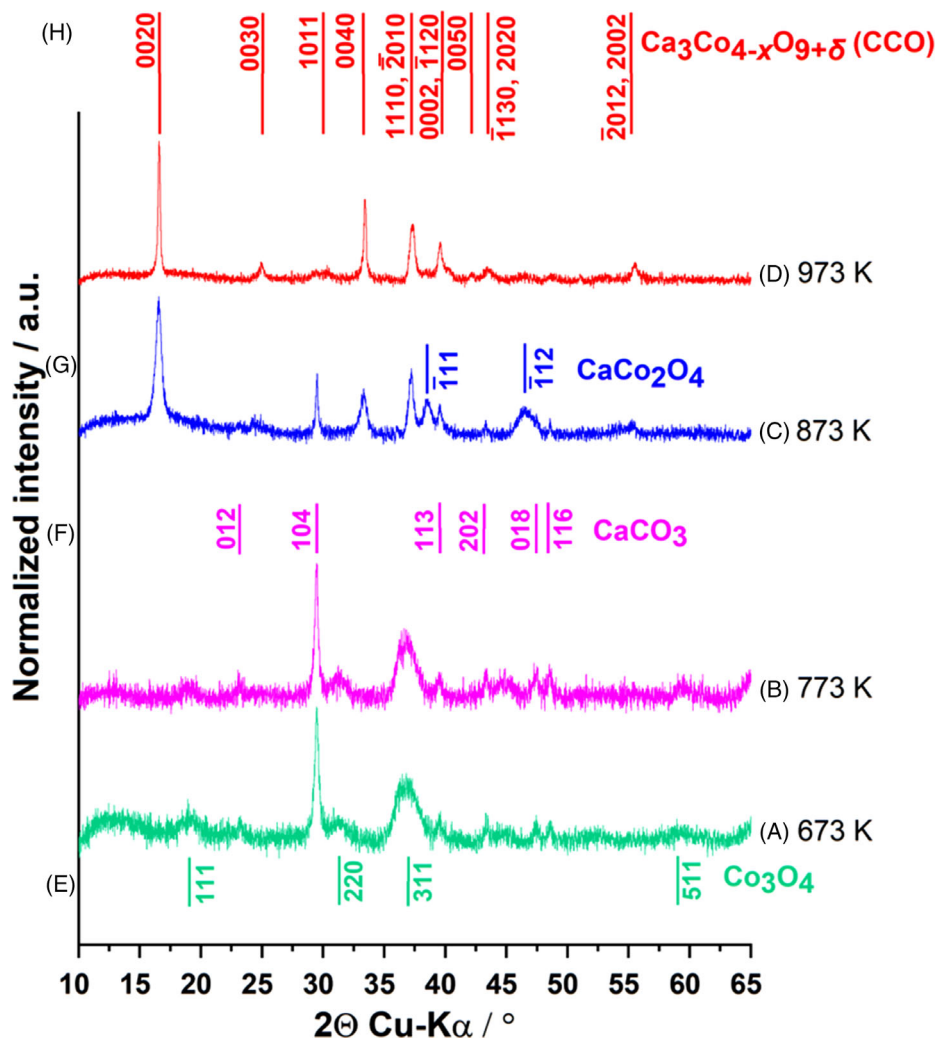


**FIGURE 1** Normalized X-ray diffraction (XRD) diffractograms of electrospun  $\text{Ca}_3\text{Co}_{4-x}\text{O}_{9+\delta}$  (CCO) nanofibers calcined at (A) 673 K, (B) 773 K, (C) 873 K, and (D) 973 K for 2 h in air. Reflections were indexed with corresponding phases: (E) cubic  $\text{Co}_3\text{O}_4$  (PDF: [01-074-1657]); (F) rhombohedral  $\text{CaCO}_3$  (PDF: [00-024-0027]); (G) monoclinic  $\text{CaCo}_2\text{O}_4$  (PDF: [00-051-1760]); (H)  $\text{Ca}_3\text{Co}_{4-x}\text{O}_{9+\delta}$ ; reflections of CCO are indexed in accordance with the four-dimensional superspace group  $Cm(0\ 1-p\ 0)$  (equivalent to  $Bm(0\ 0\ \gamma)$  (No. 8.3)) determined by Miyazaki et al.<sup>8</sup> (See also [Supporting Information](#) section for additional information on superspace group.)

Calcium cobaltite exhibits a misfit-layered structure of two interpenetrating subsystems stacked along the monoclinic  $c$ -axis. These are an electronic-conducting  $\text{CdI}_2$ -type  $\text{CoO}_2$  sheet and an oxygen deficient triple-layered rock-salt-type  $[\text{Ca}_2\text{CoO}_3]$  block that is insulating and causes phonon scattering. The combinations of the two subsystems are incommensurable parallel to their  $b$ -axis, known as  $\text{Ca}_3\text{Co}_{4-x}\text{O}_{9+\delta}$ .<sup>7–10</sup>

The chemical formula  $\text{Ca}_3\text{Co}_{4-x}\text{O}_{9+\delta}$  ( $0 \leq x \leq 0.4$ ) applied here is commonly used to refer to the non-stoichiometry of the oxygen content leading to oxygen vacancies  $\delta$  in the rock salt-type layer and of the cation ratio (Ca:Co) accompanied by different Co-valences changing  $x$  in the individual sublayers. Due to the fact that the valence state of Co is strongly influenced by the oxygen partial pressure, the stability varies depending on work conditions that include atmosphere and temperature. As

a result of the two subsystems of CCO, two different Co–O distances are involved with three different states of cobalt valences  $\text{Co}^{2+}/\text{Co}^{3+}/\text{Co}^{4+}$ , with the average value ranging from +3 to +4 depending on the variable oxygen amount. The  $\text{CoO}_2$  subsystem contains only  $\text{Co}^{3+}$  and  $\text{Co}^{4+}$ , whereas the  $\text{Ca}_2\text{CoO}_3$  subsystem also contains  $\text{Co}^{2+}$  to some degree.<sup>11–14</sup>

The TE properties of CCO are highly anisotropic.<sup>15</sup> Hence, the in-plane direction shows a high electrical conductivity within the  $[\text{CoO}_2]$  layers, whereas the out-of-plane direction shows very large phonon scattering, resulting in a low thermal conductivity.<sup>16,17</sup> Characteristics for CCO are its high Seebeck coefficient of above  $150\ \mu\text{V K}^{-1}$  and its non-toxicity.<sup>18,19</sup>

As shown in Figure S1a–c, CCO nanofibers were made by electrospinning (ES), enabling a unique microstructure in the bulk ceramic made from the nanofiber mats.<sup>20,21</sup>

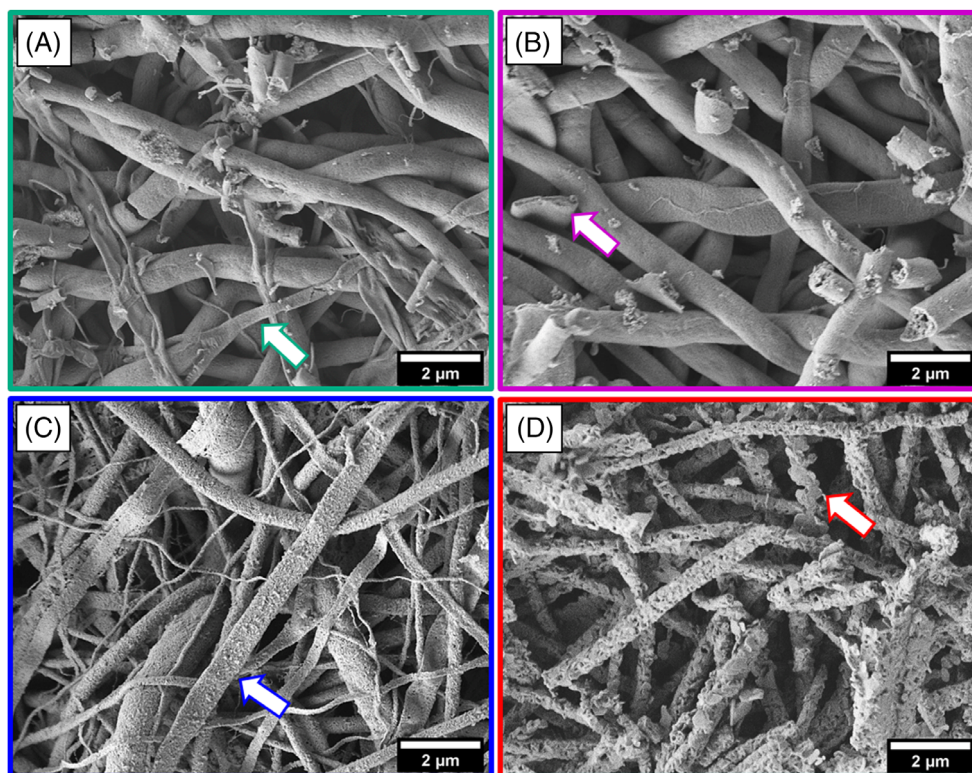


**FIGURE 2** Scanning electron microscopy (SEM) micrographs of the CCO nanofiber mats calcined at (A) 673 K, (B) 773 K, (C) 873 K, and (D) 973 K for 2 h. The arrows indicate flat nanoribbons in the mats.

Nanostructuring a material creates more interfaces, leading to enhanced phonon scattering, which affects the Seebeck coefficient and the thermal conductivity.<sup>9,22</sup> The nanofiber mats undergo calcination at medium temperature to burn out carbon residues, achieve the required CCO phase while preventing the growth of primary particles to maintain the nanostructure. The alignment of nanofibers and directional growth of their primary particles, in turn, may improve the electrical conductivity of the ceramic, due to less tortuous charge carrier mobility.<sup>23</sup> A variety of nanofiber morphologies were observed, and the emergence of which strongly depends on the interplay of calcination parameters and ES precursor composition.<sup>24,25</sup>

ES of CCO nanofibers is not new,<sup>6,9,20,26–28</sup> but only a few investigated the TE properties of this nanostructured compound. Yin et al.<sup>26</sup> combined sol-gel-based ES with spark plasma sintering (SPS) to synthesize nanocrystalline CCO ceramics. They achieved smaller particle size and improved texture in the ceramic, thereby increasing the electrical conductivity and Seebeck coefficient, and at the same time decreased the thermal conductivity compared to powder-sintered ceramics. Similarly, Sekak et al.<sup>6</sup> investigated the Seebeck coefficient of cold-pressed CCO nanofibers without sintering. However, their TE characterization was incomplete because the Seebeck

coefficient was measured only up to 300 K, and the electrical conductivity measurement was entirely excluded. This work presents a comprehensive TE characterization of cold-pressed CCO nanofibers in terms of their Seebeck coefficient and electrical conductivity up to 973 K. In addition, the TE properties of calcined nanofibers are compared to the TE properties of nanofiber-derived ceramics. Furthermore, ES is combined with in situ sintering, where sintering is performed inside the Seebeck measuring device, and the TE properties of the nanofiber-derived ceramics are determined during sintering. The advantage of using ES is the potential to create multiple interfaces within the fibers and between them. This aim can be achieved by adjusting the ES parameters to form hierarchical fibrous structure with multiple oriented interfaces on a nanometric scale. Fibers diameter, micro- and macrostructure, as well as porosity can be controlled and tailored to fit the TE requirements. In situ sintering of calcined nanofibers is potentially beneficial for mild compaction to ceramics, preserving useful features for better TE properties such as nanostructuring and interfaces as much as possible due to limited grain growth, and determining TE properties in a timely manner. We demonstrate how the thermal treatment influences the nanofibrous microstructure and to what extent it impacts the TE properties.

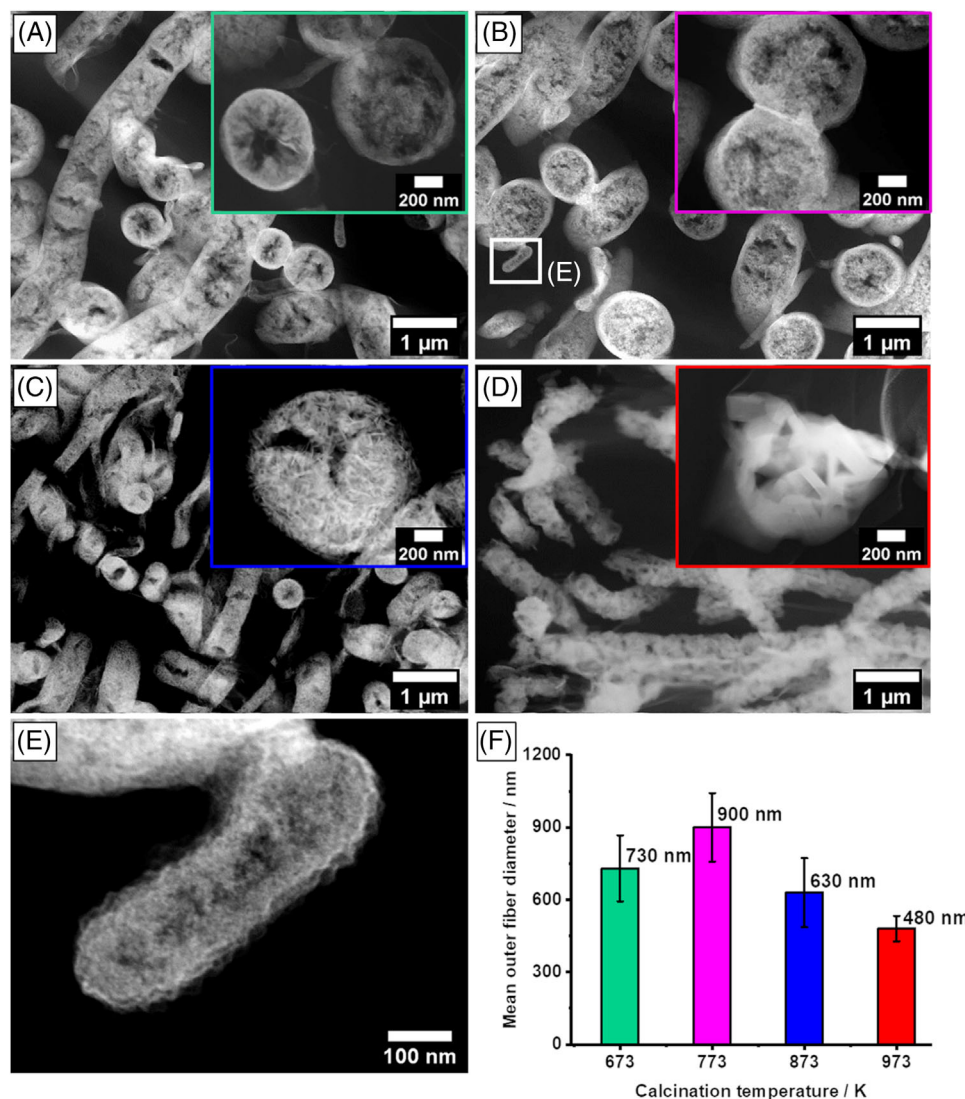


**FIGURE 3** Cross-sectional scanning transmission electron microscope (STEM) analysis in high-angle annular dark-field (HAADF) contrast of the electrospun CCO nanofiber mats calcined at (A) 673 K, (B) 773 K, (C) 873 K, and (D) 973 K for 2 h. Insets show individual cross sections of the nanofibers at higher magnification. (E) Cross section of flat nanoribbons from the 773 K calcined mat. (F) Distribution histogram of the mean outer fiber diameter of the calcined nanofibers

## 2 | EXPERIMENTAL PROCEDURES

The precursor solution consisted of 7 wt% cobalt acetate tetrahydrate ( $\text{Co}(\text{CH}_3\text{COO})_2 \cdot 4\text{H}_2\text{O}$ ) (Acros Organics, Geel, Antwerp, Belgium) that was balanced by 4 wt% calcium acetate monohydrate ( $\text{Ca}(\text{CH}_3\text{COO})_2 \cdot \text{H}_2\text{O}$ ) (Aldrich, St. Louis, MO, USA) to keep the required molar ratio (4:3) of  $\text{Ca}_3\text{Co}_{4-x}\text{O}_{9+\delta}$ . Both metal sources were mixed and stirred with propionic acid (Aldrich, St. Louis, MO, USA) (22 wt%) and absolute methanol (Bio-Lab, Jerusalem, Israel) (56 wt%) for 30 min until a homogenous purple solution was obtained. Then, polyvinylpyrrolidone (PVP) ( $M_w = 1300\,000\text{ g mol}^{-1}$ , Aldrich, St. Louis, MO, USA) was added to the solution (11 wt%) and stirred overnight. The as-prepared precursor solution ( $\sim 350\text{ cPs}$ )

was electrospun (NS 24, Inovenso, Turkey) under the applied voltage of 25 kV, with a tip to collector distance of 12 cm and a precursor feed rate of  $1\text{ ml h}^{-1}$ . The relative humidity inside the system container was 45%, and the temperature was 293–303 K. The fibers' mats were collected on an aluminum foil taped to the drum collector.

After ES, the fiber-coated aluminum foils were dried overnight in a preheated furnace (353 K). Subsequently, the mats were peeled off the aluminum foil, cut to  $\sim 2 \times 2\text{ cm}^2$  squares, and finally calcined at 673, 773, 873, and 973 K for 2 h (see Figures S2 and S3). The calcined nanofiber mats were characterized by X-ray diffraction (XRD, Bruker D8 Advance) with  $\text{Cu-K}\alpha$  radiation at 30 kV and 40 mA. The microstructure of the nanofiber mats was investigated via

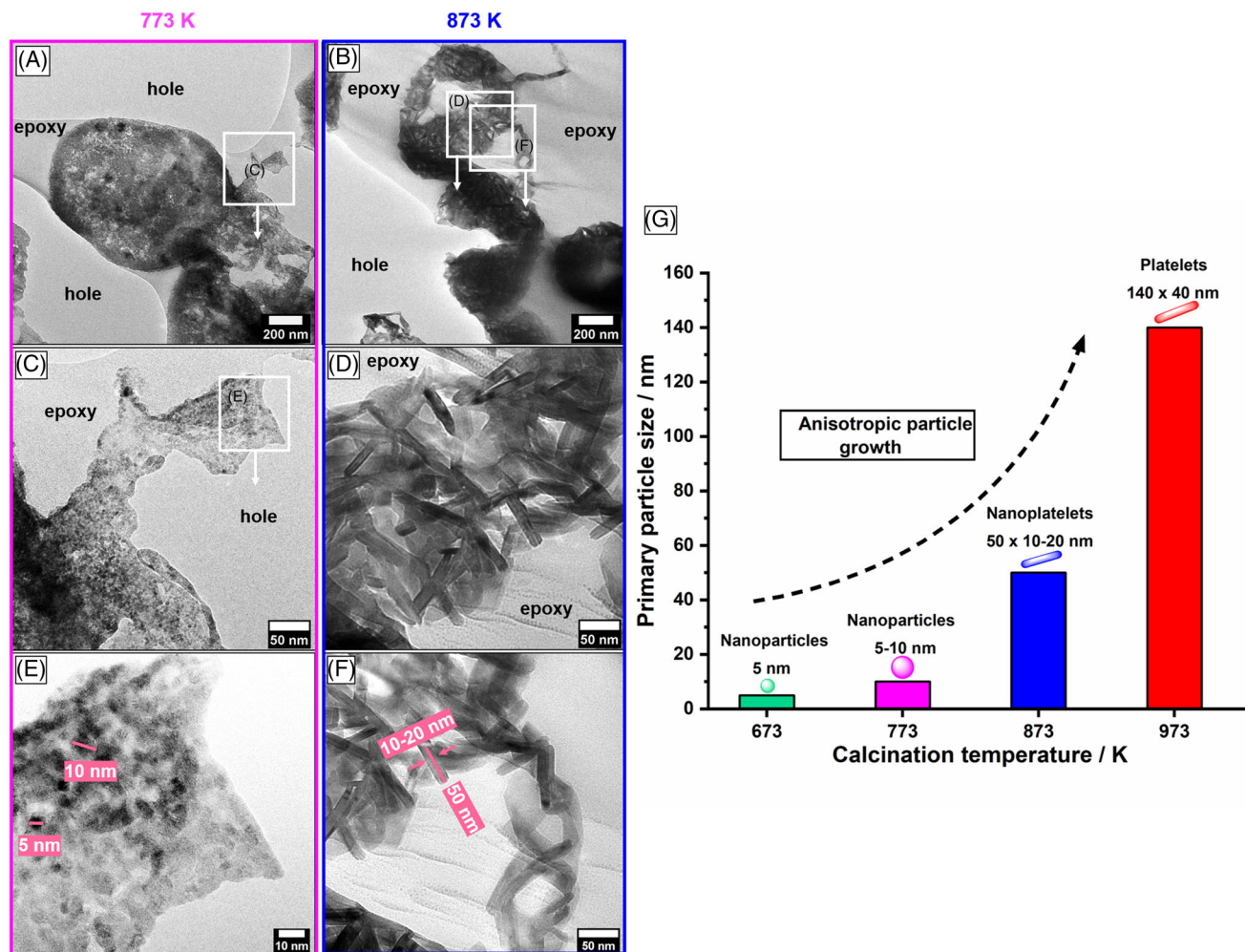


**FIGURE 4** Cross-sectional transmission electron microscopy (TEM) bright-field characterization shows the change in size and morphology of the electrospun CCO nanofibers in the samples calcined at (A) 773 K and (B) 873 K. Magnified TEM bright-field micrographs of the electrospun CCO nanofibers calcined at (C) 773 K and (D) 873 K. For the different magnifications, sites of the nanofiber cross sections were selected that are highly thinned out to make the primary particles more visible. Areas of epoxy resin and the holes created during argon-ion polishing were identified by their different contrasts. In addition, size values of a few particles of the corresponding samples (E) 773 K and (F) 873 K are shown. (G) Overview of the anisotropic particle growth in the calcined nanofibers along the increase of the calcination temperature from nanoparticles to nanoscale platelets

field-emission scanning electron microscopy (FE-SEM, JEOL JSM-6700F), combined with an energy-dispersive X-ray spectrometer (EDXS, Oxford Instruments INCA 300) and by FE transmission electron microscopy (FE-TEM, JEOL JEM-2100F-UHR), outfitted with an EDX spectrometer (Oxford Instruments INCA 200 TEM) and a Gatan Imaging Filter (GIF 2001). For TEM, the nanofiber mats were embedded in epoxy resin, polished from both sides on diamond lapping films using the MultiPrep system (Allied High Tech Products, Inc.) and subsequently 3 kV argon-ion polished with a Precision Ion Polishing System (Gatan-Model 691) to electron transparency. The TEM investigation was made at 200 kV, and the FE-TEM was operated in a scanning transmission electron microscope (STEM) mode in high-angle annular dark-field (HAADF)

contrast. TEM bright-field, high-resolution TEM (HRTEM), and selected area electron diffraction (SAED) were also applied. Density and porosity of calcined nanofiber bodies (see Figure S1) and sintered nanofiber bulk ceramics were determined by the Archimedes method (ISO 5018:1983) as stated in the [Supporting Information](#) section, in which the dry mass, mass in solvent, and wet mass of the sample were determined. Isopropanol was used as the liquid, and a theoretical density of  $4.68 \text{ g cm}^{-3}$  was used for CCO.

For the TE characterization, the calcined nanofiber mats were grounded gently and cold pressed in a bar-shaped die ( $10 \text{ mm} \times 4 \text{ mm} \times 1 \text{ mm}$ ) at 500 MPa for 20 min to form the calcined nanofiber body (see Figure S1c). The Seebeck coefficient and electrical conductivity were measured

perpendicular to the pressing direction. For comparison, a commercial CCO powder (particle size up to  $1\ \mu\text{m}$ ) was purchased from CerPoTech (Tiller, Norway). The powder was also pressed into a bar and calcined at 973 K for 2 h. The Seebeck coefficient was measured in a ProboStat A setup (NorECs) with a vertical furnace (Elite Thermal System) and Digital-Multimeters (Keithley 2100 6/12). The temperature program for the different nanofiber mats and the reference powder (comparative sample) included heating to the previously used calcination temperature (673, 773, 873, and 973 K) with a heating rate of  $3\ \text{K min}^{-1}$  and cooling steps of 100 K with a dwell time of 2 h to 373 K, as shown in Figure S1c. All values were recorded after heating to the particular maximum temperature. Afterward, the samples were subjected to in situ sintering at 1073 K for 2 h with a heating rate of  $3\ \text{K min}^{-1}$  within the furnace of the Seebeck coefficient apparatus to obtain the ceramics. Analysis of the electrical conductivity was performed by a 4-point probe method, in a tube furnace (Carbolite Gero EVZ 12/450B). Subsequent measurements were carried out with the temperature program described previously and displayed in Figure S1c.

### 3 | RESULTS AND DISCUSSION

The calcined electrospun nanofiber mats were examined by XRD, as shown in Figure 1. At 673 and 773 K, only  $\text{Co}_3\text{O}_4$  and  $\text{CaCO}_3$  are observed. The broad reflections in the diffractograms (Figure 1A,B), with small intensities and low signal-to-noise ratios, reveal the nanocrystallinity of the particles. Formation of the CCO phase occurs at 873 K (Figure 1C) and is linked to the decomposition of  $\text{CaCO}_3$  and its coalescence with  $\text{Co}_3\text{O}_4$ , as described by Bittner et al.<sup>29</sup> In addition to CCO, the intermediate phase  $\text{CaCo}_2\text{O}_4$  formed, which also has a layered crystal structure in which  $[\text{CoO}_2]_n$  layers are stacked with  $\text{Ca}^{+}$ -ion layers.<sup>27</sup> Furthermore, the 104, 202, and 116 reflections of rhombohedral  $\text{CaCO}_3$  are still present at 873 K (Figure 1C), suggesting that the decomposition and incorporation of  $\text{CaCO}_3$  as well as the transformation to CCO was incomplete. At 973 K (Figure 1D), the intermediate phases  $\text{CaCo}_2\text{O}_4$  and  $\text{CaCO}_3$  disappear, leaving CCO as the only compound in the nanofibers. Closer examination of the  $2\theta$ -regions around the 220 reflections of  $\text{Co}_3\text{O}_4$  and 116 of  $\text{CaCO}_3$  also prove that both phases are clearly no longer present in the 973 K sample (diffractograms can be found in Figure S4). The corresponding XRD diffractogram in Figure 1D shows a higher signal-to-noise ratio, and the reflection width is narrower than at lower temperatures, indicating particle growth with increasing temperature. In fact, the intensities of the reflections, especially the 0020 and 0040

CCO reflections, are more pronounced, indicating some texturing within the nanofibers.

The morphology of the electrospun CCO nanofiber mats after thermal treatment was analyzed by SEM (see Figure 2) and showed flat and curved nanofibers arranged randomly.

After calcination at 673 and 773 K, the nanofibers have a nanograined surface, but no distinct particles, as illustrated in Figure 2A,B. At 873 K, the nanofiber surface coarsens with flat particles, which further increase in size at 973 K. These platelet-like particles likely belong to CCO, because of its layered crystal structure.<sup>26</sup> The results from the XRD analysis support the observations from the SEM micrographs. Additionally, each calcined nanofiber mat also possesses flat nanoribbons, indicated by arrows in Figure 2. Due to their flatness, nanoribbons are expected to pack more efficiently compared to cylindrical nanofibers, enabling a higher green body density in the bulk ceramic, allowing milder sintering conditions.<sup>30</sup> Furthermore, they can introduce more interfaces into the final bulk ceramic, which can improve the functional properties of the material. Therefore, it is beneficial to produce such nanoribbons.

To understand the influence of the thermal treatment on the nanocrystalline structure, the calcined nanofiber mats were examined by TEM measurements (Figure 3). The STEM-HAADF micrographs show cross-sectional views of the calcined CCO nanofiber mats. At 673 and 773 K (Figure 3A,B), a mixture of hollow and core-shell (solid) nanofibers was elucidated. The nanofibers' mats calcined at 873 K (Figure 3C) and 973 K (Figure 3D) mainly contain a porous nanofiber structure. These nanofibers clearly consist of platelet-like particles that arrange in the nanofibrous confinement. Moreover, the EDXS element mappings for O (green), Ca (red), and Co (blue) in Figure S5 show that the CCO nanofiber mat calcined at 973 K has a homogenous elemental distribution with no separated phases. As also determined before via XRD measurements (Figure 1D), the CCO phase was produced here without impurities. For the determination of the nanofiber diameter, a distribution histogram of the mean outer nanofiber diameter (Figure 3F) was obtained from about 100 measured nanofiber diameters for each calcination temperature. Interestingly, the outer nanofiber diameter passes through a maximum at 773 K and is about 480 nm at 973 K, which is smaller by half compared to the nanofibers calcined at lower temperatures. This is related to the oxidative decomposition of the polymer PVP and the metal precursors as well as the resulting gas evolution, causing first an expansion and then a shrinkage of the nanofiber diameter after all organic components are eliminated.<sup>24</sup> The cross sections of the nanofibers are mostly circular, but

cross sections of flat nanoribbons could also be observed, as shown in Figure 4E.

Flat nanoribbons are formed during ES via the following steps: (1) formation of dry polymer skin around the liquid jet, (2) solvent evaporation from the core of the cylindrical fiber through the tubular skin, and (3) tube collapse to form a flat ribbon.<sup>31,32</sup> As the ES process is largely affected by many parameters (described earlier), a mixture of nanoribbons and cylindrical nanofibers are present in our mats.

Furthermore, the microstructure of the nanofibers was analyzed using TEM bright-field (Figure 4A–E). The focus was on the nanofiber mats calcined at 773 and 873 K, as the transition from the intermediate phases to the CCO phase was determined by XRD and SEM analysis to occur between these two temperatures. Closer inspection of the nanofibers shows again a clear transition from core-shell to porous structure. The morphology of the primary particles shifts from nanoparticles with a diameter of 5–10 nm to nanoplatelets with a width of 50 nm and a thickness of 10–20 nm. The nanoplatelets obtained here are significantly smaller than the CCO platelets fabricated by Sekak et al.<sup>6</sup> at 923 K (width: 80–150 nm, thickness: 20–40 nm), whose nanofibers had already transformed into linked particles. As shown in Figure 4E, an anisotropic growth of the primary particles in the nanofibers occurs at higher calcination temperature (see the particle size of nanofibers calcined at 673 and 973 K in Figure S6). Platelets are the characteristic of the CCO phase due to the layered crystal structure, and their appearance is consistent with the formation of CCO at 873 K (Figure 1), the SEM micrographs (Figure 2C,D), and the STEM-HAADF micrographs (Figure 3E,F). The nanocrystalline particles and nanoplatelets in the TEM bright-field micrographs (Figure 4C,D) are randomly aligned in the nanofibers as the contrast of the particles differs from each other, revealing their polycrystalline nature.

Further analysis concerning the phase identification, the primary particle size and the polycrystallinity of the electrospun CCO nanofiber mats calcined at 873 and 973 K were conducted by TEM bright-field, HRTEM, and SAED measurements in Figure 5. Clearly apparent in Figure 5A, the nanofibers calcined at 873 K are composed of a variety of nanoplatelets that stay in the geometric confinement of the nanofibers and show no directional alignment as also found in the STEM results. The HRTEM micrographs reveal a platelet (Figure 5C) of CCO with a width of 140 nm and a thickness of ~40 nm in the nanofiber mat calcined at 973 K. The particle size of 40 nm was also achieved by Yin et al.<sup>26</sup> in electrospun CCO nanofibers, however, at slightly higher temperature (1023 K). The higher magnified HRTEM micrographs (Figure 5E,F) show the

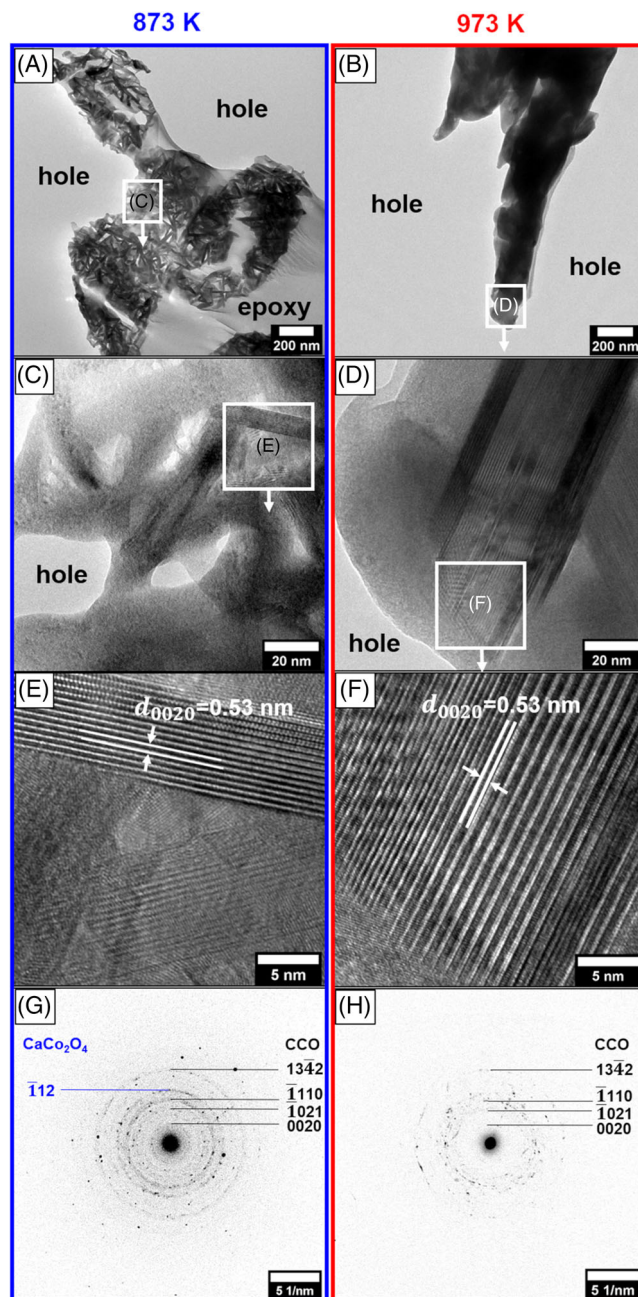


**FIGURE 5** Cross-sectional transmission electron microscopy (TEM) bright-field micrographs of the electrospun CCO nanofibers calcined at (A) 873 K and (B) 973 K for 2 h, (C)–(F) high-resolution transmission electron microscopy (HRTEM), (G and H) selected area electron diffraction (SAED) polycrystalline ring pattern of CCO nanofibers calcined at 873 and 973 K

corresponding lattice planes of the particles of the CCO phase. The measured lattice spacings of the stacked layers are both 0.53 nm and thus can be identified as (0020) planes of CCO, proving the crystallization of the CCO phase at these temperatures. The SAEDs in Figure 5G,H (see also rotational averaged SAEDs in Figure S7) predominantly display ring patterns, confirming the

**TABLE 1** Relative density, closed porosity, Seebeck coefficient, and electrical conductivity of the calcined and in situ sintered (1073 K) CCO nanofiber bodies and CCO reference powder (comparative sample)

Samples		Relative density (%)	Closed porosity (%)	Seebeck coefficient ( $\mu\text{V K}^{-1}$ )	Electrical conductivity ( $\text{S cm}^{-1}$ )
Calcination (K)	In situ sintering (K)				
873	–	46.9	19.4	198.5	20.1
873 <sup>a</sup>	1073	62.7	1.2	169.4	69.1
973	–	62.5	4.7	175.6	52.8
973 <sup>a</sup>	1073	65.3	4.8	176.5	83.7
973 (comp. sample)	–	63.2	4.6	172.9	70.6
973 (comp. sample)	1073	66.9	0.4	165.0	102.6

<sup>a</sup>Sintered nanofiber bulk ceramics (see Figure S1).

polycrystallinity, fine particle sizes, and random particle orientation distribution in the nanofibers. As CCO exhibits a misfit-layered composite crystal structure with two subsystems having incommensurable lattice parameters  $b_1$  and  $b_2$ , the indexing of these diffraction patterns was realized with the four-dimensional superspace group  $Cm(0\ 1 - p\ 0)$  (equivalent to  $Bm(0\ 0\ \gamma)$  (No. 8.3)) in accordance with Miyazaki et al.,<sup>8</sup> which better describes the symmetry of the structure and was also used for the evaluation of the XRD diffractograms. For more details regarding the superspace group, we kindly refer the reader to the [Supporting Information](#) section and the literature sources given there. For the nanofiber mat calcined at 873 K, a diffraction of  $\text{CaCo}_2\text{O}_4$  was also identified in the SAED pattern, analogously to the findings of the XRD analysis. Accordingly, 973 K can be considered a suitable calcination temperature to generate pure CCO nanofibers with small primary particles.

The influence of the nanofiber structure on the TE properties was investigated by measuring the electrical conductivity and the Seebeck coefficient. The properties of bodies from nanofibers calcined at 873 and 973 K are compared to nanofiber bodies that had undergone in situ sintering at 1073 K, where the bar-shaped samples are sintered during the measurement process (for characterization of nanofibers calcined at 673 and 773 K, see Figure S8). In addition, a CCO reference powder with particle sizes up to  $1\ \mu\text{m}$  was used for comparison. All samples were cold-pressed into bars to achieve adequate sample compactness. The reference powder was also calcined at 973 K, cold-pressed, and in situ sintered at 1073 K. The electrical conductivity of the calcined CCO nanofibers rises with increasing calcination temperature (Figure 6A). At 873 K, the electrical conductivity of samples calcined at 873 and 973 K was  $20.1$  and  $52.8\ \text{S cm}^{-1}$ , respectively (see Table 1). However, the calcined nanofiber bodies exhibit lower

electrical conductivity than the sintered nanofiber bulk ceramics. This can be explained by the more pronounced densification of the CCO nanofibers during in situ sintering at 1073 K, resulting in a more compact structure. Furthermore, Figure 7A–D shows that from the calcined pressed body to the sintered ceramic, the nanofiber morphology gets lost and the particle size increases. Although the pressed nanofibers initially have a diameter of up to  $1\ \mu\text{m}$ , particles with this size ratio are found in the sintered ceramics. This suggests that it is not the fibrous continuity along the fiber axis, and thus the electrical contact of the grains in the fibers, which favors the electrical conductivity here, but rather the additional particle growth and densification during sintering that contribute to the higher electrical conductivity.

For comparison, the values at the measurement temperature of 873 K were contrasted with the measured relative densities in Table 1. Higher density gives rise to higher electrical conductivity, whereas higher porosity typically leads to an opposite effect. A possible explanation of the effect of porosity could be that the internal surface in the porous material increases the charge scattering at the material boundaries and interfere with the charge transport, which affects the electrical conductivity.<sup>33</sup> Moreover, the CCO reference powder generally features higher electrical conductivity than the nanofibers, both in the calcined and in situ sintered states. Density measurements indicate slightly higher densification for the commercial CCO powder. In Figure 7C–F, it can be seen that the particle size of the commercial CCO powder is not much different from those of the nanofiber ceramics. However, as the inset in Figure 7F shows, lamellar arrangements of the platelets can be observed in the CCO powder ceramic, suggesting the presence of a texture. The assumption of texture is supported by the XRD diffractograms of the in situ sintered samples in Figure S9. The diffractogram of

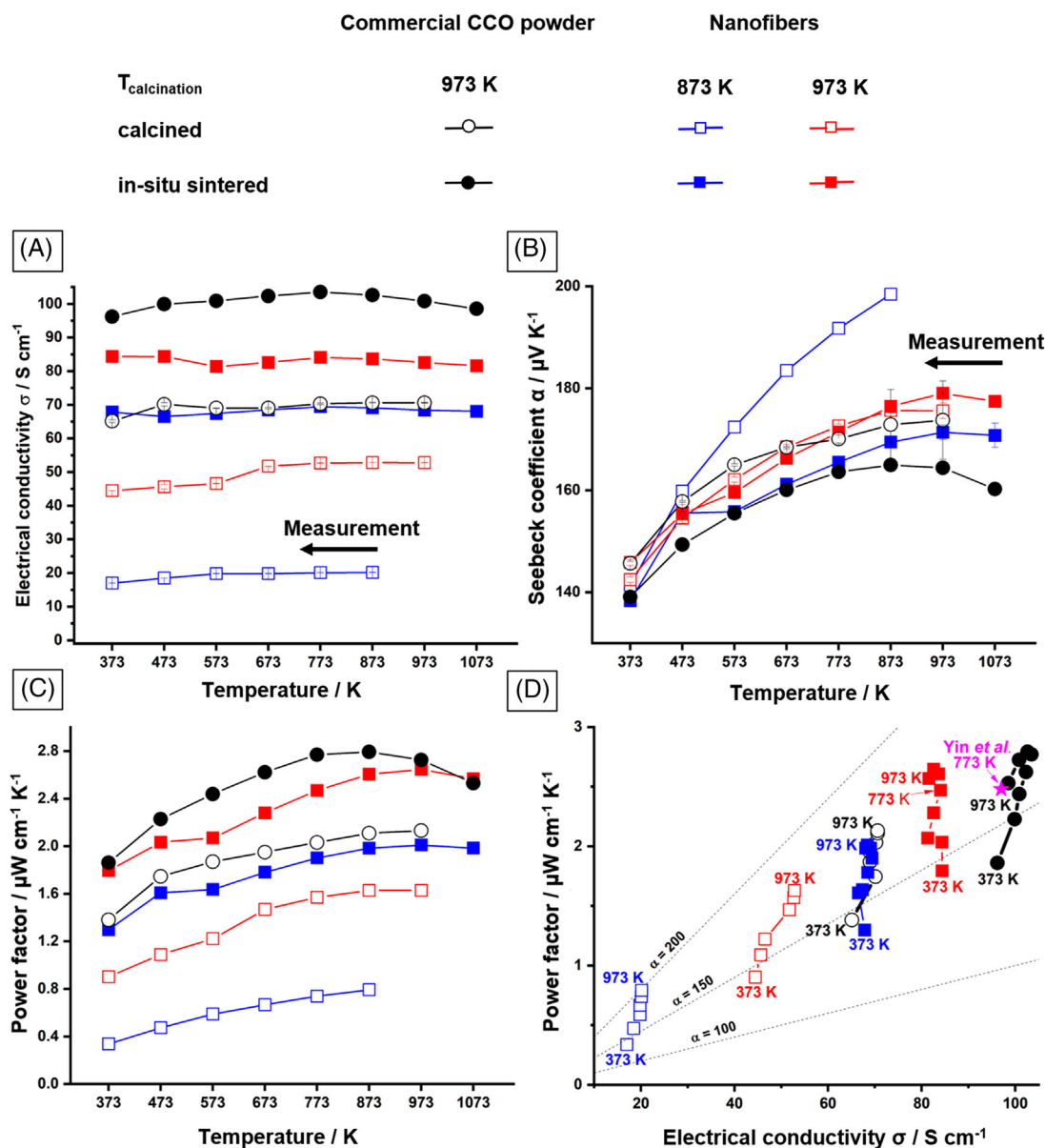


**FIGURE 6** Thermoelectric characterization of calcined and in situ sintered CCO nanofibers and commercial CCO powder: (A) electrical conductivity, (B) Seebeck coefficient, (C) resulting power factor, and (D) type-I Ioffe plot with the power factor against the electrical conductivity

the sintered CCO powder ceramics shows a shift in the intensity of the 0020 and 0040 reflections compared to the sintered nanofiber ceramics, and the 1011 reflection is completely absent, implying an orientation of the platelets in the ceramics, which might additionally favor electrical conductivity.

The Seebeck coefficient behaves quite similarly for all samples except for the nanofibers calcined at 873 K (see Figure 6B). Higher Seebeck coefficients are obtained with increasing porosity at elevated temperatures (see Table 1). In particular, nanofibers calcined at 873 K exhibit a relatively high porosity of 19.4%, leading to the distinct increase of the Seebeck coefficient in Figure 6B. The

enhancement in Seebeck coefficient due to porosity is ascribed to energy filtering, phonon drag, and pore scattering effects.<sup>33,34</sup> As Valalaki et al.<sup>33</sup> emphasized, the Seebeck coefficient results from the diffusion of charge carriers along a temperature gradient. It can be increased by charge carrier-phonon scattering at pores and interfaces, effecting more the low-energy charge carriers.<sup>34</sup> Considering that nanoribbons provide more interfaces to the ceramic structure, they also contribute to the Seebeck coefficient.

The corresponding power factor at 873 K in Figure 6C shows a slightly improved value of  $2.57 \mu\text{W cm}^{-1} \text{K}^{-2}$  at 1073 K for the in situ sintered ceramic of nanofibers calcined at 973 K compared to  $2.53 \mu\text{W cm}^{-1} \text{K}^{-2}$  for

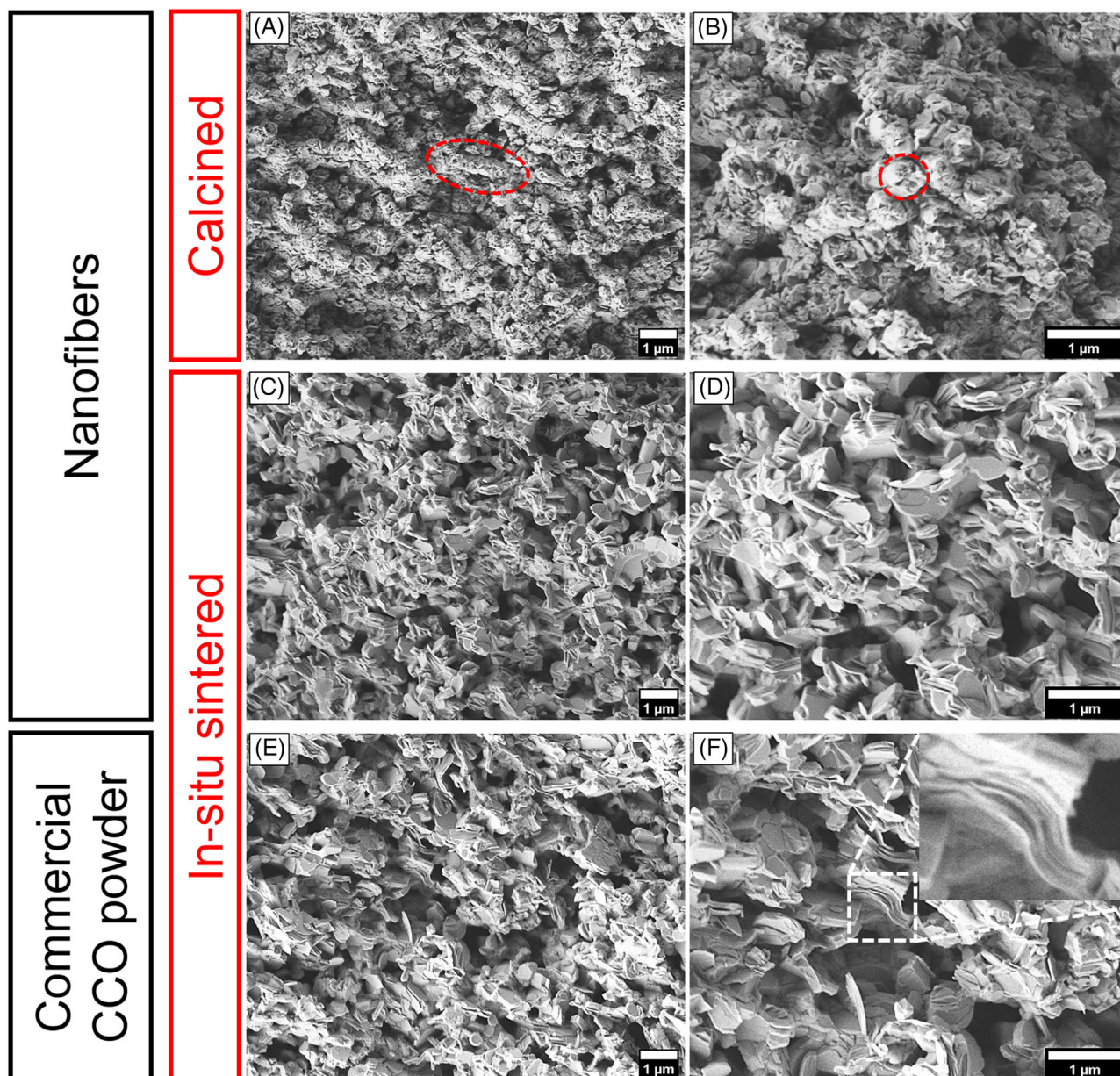


**FIGURE 7** Cross-sectional scanning electron microscope (SEM) micrographs of (A and B) the cold-pressed nanofiber body calcined at 973 K (dashed red circles show nanofibers horizontal and vertical to the cross section), at 1073 K in situ sintered (C and D) nanofiber-derived bulk ceramic pre-calcined at 973 K, and (E and F) the ceramic of the commercial CCO powder with the inset showing lamellar arrangement of platelets

the ceramic of the CCO reference powder. The ceramic nanofiber does not have higher electrical conductivity, but its nanostructuring and higher porosity result in higher Seebeck coefficients, which in turn helps to balance the power factor. For comparison, the differences of the in situ sintering process were compared to the work of Yin et al.,<sup>26</sup> who also synthesized electrospun CCO nanofibers, but sintered them using SPS. In Figure 6D, referred to as type-I Ioffe plot, the power factor is plotted as a function of the electrical conductivity. The reference value from Yin et al. is marked here with an asterisk and is from the

measurement at 773 K. Despite using the in situ sintering method, the power factor in this work of  $2.47 \mu\text{W cm}^{-1} \text{K}^{-2}$  at 773 K for the nanofiber ceramic calcined at 973 K and sintered at 1073 K is similar to the value of  $2.48 \mu\text{W cm}^{-1} \text{K}^{-2}$  for the CCO nanofiber ceramic prepared by SPS at 1023 K. The similar power factor  $\sigma\alpha^2$  is related to the fact that, unlike the SPS ceramic, no adequate texturing was established into the ceramic, resulting in an electrical conductivity that was about 13% lower. Looking closely at the SEM micrograph in Figure 7C,D, it is apparent that the ceramic in this work has no real texturing after sintering,

as the particles are randomly arranged, and no alignment is visible. This could be due to the fact that a pressureless sintering process was used and, thus, grain rotation was not facilitated due to the pores in the bulk ceramic, as was the case with SPS.<sup>26</sup> In contrast, a 10% higher Seebeck coefficient was realized owing to the enhanced porosity of the pressed nanofibers and the ceramics obtained by in situ sintering, yielding similar power factors.

## 4 | CONCLUSIONS


Nanocrystalline CCO nanofibers and nanoribbons have been fabricated by sol-gel-based ES and compacted to nanofiber-derived ceramics using an in situ sintering technique, where the sintering takes place inside the Seebeck measurement device. Detailed characterization of the calcined nanofibers shows a pronounced dependence of the microstructure on the synthesis parameters and calcination temperature. The appearance of nanoribbons coincides with the previous formation of hollow nanofibers. Increased Seebeck coefficient at high temperature is obtained in calcined CCO nanofibers due to smaller particle sizes and more porosity in the structure. However, despite their nanofibrous continuity, they exhibit lower electrical conductivity than sintered ceramics, because density evidently contributes more to electrical conductivity. The in situ sintering yielded a comparable power factor to the SPS-sintered CCO nanofiber ceramics of Yin et al.<sup>26</sup> but with improved Seebeck coefficient, which is desirable for high-temperature applications where high power output is required. The performance of our nanofiber-derived ceramics may be further enhanced by subjecting the in situ sintered samples to a final SPS treatment that additionally consolidates the material.<sup>26</sup> The improved Seebeck coefficient can pave the way for the use of the electrospun CCO samples in high-temperature power generation technologies such as the recovery of wasted thermal energy.

## ACKNOWLEDGMENTS

This work was financially supported by the Ministry of Science and Culture of Lower Saxony (MWK) in the frame of the Research Cooperation Lower Saxony-Israel. The work was supported by the Nancy & Stephan Grand Technion Energy Program (GTEP); GSG acknowledges the support of the Arturo Gruenbaum Chair in Materials Engineering. This research was supported by the Israeli Ministry of Energy as part of the scholarship's program for first to third degree students in the fields of energy.

Open access funding enabled and organized by Projekt DEAL.

## ORCID

Katharina Kruppa  <https://orcid.org/0000-0002-3764-2109>

Gideon S. Grader  <https://orcid.org/0000-0003-4371-4575>

Armin Feldhoff  <https://orcid.org/0000-0003-1599-432X>

## REFERENCES

1. Hudak NS, Amatucci GG. Small-scale energy harvesting through thermoelectric, vibration, and radiofrequency power conversion. *J Appl Phys*. 2008;103(10):101301. <https://doi.org/10.1063/1.2918987>
2. Feldhoff A. Thermoelectric material tensor derived from the Onsager-de Groot-Callen model. *Energy Harvest Syst*. 2015;2(1-2):5-13. <https://doi.org/10.1515/ehs-2014-0040>
3. Wolf M, Hinterding R, Feldhoff A. High power factor vs. high zT—a review of thermoelectric materials for high-temperature application. *Entropy*. 2019;21(11):1058. <https://doi.org/10.3390/e21111058>
4. Kanas N, Singh SP, Rotan M, Liu Z, Fan Z, Chen L, et al. Influence of processing on stability, microstructure and thermoelectric properties of  $\text{Ca}_3\text{Co}_{4-x}\text{O}_{9+\delta}$ . *J Eur Ceram Soc*. 2018;38(4):1592-9. <https://doi.org/10.1016/j.jeurceramsoc.2017.11.011>
5. Koumoto K, Funahashi R, Guilmeau E, Miyazaki Y, Weidenkaff A, Wang Y, et al. Thermoelectric ceramics for energy harvesting. *J Am Ceram Soc*. 2013;96(1):1-23. <https://doi.org/10.1111/jace.12076>
6. Sekak KA, Lowe A. Structural and thermal characterization of calcium cobaltite electrospun nanostructured fibers. *J Am Ceram Soc*. 2011;94(2):611-9. <https://doi.org/10.1111/j.1551-2916.2010.04106.x>
7. Wu L, Meng Q, Jooss C, Zheng J-C, Inada H, Su D, et al. Origin of phonon glass-electron crystal behavior in thermoelectric layered cobaltate. *Adv Funct Mater*. 2013;23(46):5728-36. <https://doi.org/10.1002/adfm.201301098>
8. Miyazaki Y, Onoda M, Oku T, Kikuchi M, Ishii Y, Ono Y, et al. Modulated structure of the thermoelectric compound  $[\text{Ca}_2\text{CoO}_3]_{1.62}\text{CoO}_2$ . *J Phys Soc Jpn*. 2002;71(2):491-97. <https://doi.org/10.1143/JPSJ.71.491>
9. Ou Y, Zou D, Wang F, Cheng J. Effect of synthesis parameters on the morphology of nanocrystal thermoelectric M( = Mg, Mn, Cu) doped  $\text{Ca}_3\text{Co}_4\text{O}_9$  fibers by electrospinning. *Mater Today Proc*. 2018;5(12):25900-5. <https://doi.org/10.1016/j.matpr.2018.07.111>
10. Lambert S, Leligny H, Grebille D. Three forms of the misfit layered cobaltite  $[\text{Ca}_2\text{CoO}_3][\text{CoO}_2]_{1.62}$ : A 4D structural investigation. *J Solid State Chem*. 2001;160(2):322-31. <https://doi.org/10.1006/jssc.2001.9235>
11. Kanas N, Skomedal G, Desissa TD, Feldhoff A, Grande T, Wiik K, et al. Performance of a thermoelectric module based on n-type  $(\text{La}_{0.12}\text{Sr}_{0.88})_{0.95}\text{TiO}_{3-\delta}$  and p-type  $\text{Ca}_3\text{Co}_{4-x}\text{O}_{9+\delta}$ . *J Electron Mater*. 2020;49(7):4154-9. <https://doi.org/10.1007/s11664-020-08127-5>
12. Zhou XD, Pederson LR, Thomsen E, Nie Z, Coffey G. Non-stoichiometry and transport properties of  $\text{Ca}_3\text{Co}_{4\pm x}\text{O}_{9+\delta}$  ( $x = 0-0.4$ ). *Electrochem Solid State Lett*. 2009;12(2):2008-10. <https://doi.org/10.1149/1.3039948>

13. Shimoyama JI, Horii S, Otszchi K, Sano M, Kishio K. Oxygen nonstoichiometry in layered cobaltite  $\text{Ca}_3\text{Co}_4\text{O}_y$ . *Jpn J Appl Phys.* 2003;42(2B):L194. <https://doi.org/10.1143/JJAP.42.L194>
14. Delorme F, Diaz-Chao P, Guilmeau E, Giovannelli F. Thermoelectric properties of  $\text{Ca}_3\text{Co}_4\text{O}_9$ - $\text{Co}_3\text{O}_4$  composites. *Ceram Int.* 2015;41(8):10038–43. <https://doi.org/10.1016/j.ceramint.2015.04.091>
15. Butt S, Xu W, He WQ, Tan Q, Ren GK, Lin Y, et al. Enhancement of thermoelectric performance in Cd-doped  $\text{Ca}_3\text{Co}_4\text{O}_9$  via spin entropy, defect chemistry and phonon scattering. *J Mater Chem A.* 2014;2(45):19479–87. <https://doi.org/10.1039/c4ta03891f>
16. Sun T, Hng HH, Yan QY, Ma J. Enhanced high temperature thermoelectric properties of Bi-doped c-axis oriented  $\text{Ca}_3\text{Co}_4\text{O}_9$  thin films by pulsed laser deposition. *J Appl Phys.* 2010;108(8):1–6. <https://doi.org/10.1063/1.3499324>
17. Lim CH, Seo WS, Lee S, Lim YS, Kim J-Y, Park H-H, et al. Anisotropy of the thermoelectric figure of merit (ZT) in textured  $\text{Ca}_3\text{Co}_4\text{O}_9$  ceramics prepared by using a spark plasma sintering process. *J Korean Phys Soc.* 2015;66(5):794–799. <https://doi.org/10.3938/jkps.66.794>
18. Aksit M, Kolli SK, Slauch IM, Robinson RD. Misfit layered  $\text{Ca}_3\text{Co}_4\text{O}_9$  as a high figure of merit p-type transparent conducting oxide film through solution processing. *Appl Phys Lett.* 2014;104(16):3–7. <https://doi.org/10.1063/1.4871506>
19. Kenfaui D, Gomina M, Noudem JG, Chateigner D. Anisotropy of transport properties correlated to grain boundary density and quantified texture in thick oriented  $\text{Ca}_3\text{Co}_4\text{O}_9$  ceramics. *Materials (Basel).* 2018;11(7):1224. <https://doi.org/10.3390/ma11071224>
20. Qiu Z, Pei J, Chen G, Lv C, Zhang Y, Yu Y, et al. Electrospinning technique synthesis and electrical performances of one dimensional  $\text{Ca}_2\text{Co}_2\text{O}_5$  with hierarchical structure. *Mater Lett.* 2015;158:182–5. <https://doi.org/10.1016/j.matlet.2015.06.014>
21. Esfahani H, Jose R, Ramakrishna S. Electrospun ceramic nanofiber mats today: synthesis, properties, and applications. *Materials (Basel).* 2017;10(11):1238. <https://doi.org/10.3390/ma10111238>
22. Ma F, Ou Y, Yang Y, Liu Y, Xie S, Li J-F, et al. Nanocrystalline structure and thermoelectric properties of electrospun  $\text{NaCo}_2\text{O}_4$  nanofibers. *J Phys Chem C.* 2010;114(50):22038–43. <https://doi.org/10.1021/jp107488k>
23. Prasad R, Bhame SD. Review on texturization effects in thermoelectric oxides. *Mater Renew Sustain Energy.* 2020;9(1):3. <https://doi.org/10.1007/s40243-019-0163-y>
24. Elishav O, Beilin V, Shter GE, Dinner O, Halperin V, Grader GS. Formation of core-shell mesoporous ceramic fibers. *J Am Ceram Soc.* 2017;100(8):3370–4. <https://doi.org/10.1111/jace.15022>
25. Mann-Lahav M, Halabi M, Shter GE, Beilin V, Balaish M, Ein-Eli Y, et al. Electrospun ionomeric fibers with anion conducting properties. *Adv Funct Mater.* 2020;30(18):1–11. <https://doi.org/10.1002/adfm.201901733>
26. Yin T, Liu D, Ou Y, Ma F, Xie S, Li J-F, et al. Nanocrystalline thermoelectric  $\text{Ca}_3\text{Co}_4\text{O}_9$  ceramics by sol-gel based electrospinning and spark plasma sintering. *J Phys Chem C.* 2010;114(21):10061–5. <https://doi.org/10.1021/jp1024872>
27. Li L, Peng S, Cheah Y, Ko Y, Teh P, Wee G, et al. Electrospun hierarchical  $\text{CaCo}_2\text{O}_4$  nanofibers with excellent lithium storage properties. *Chemistry – A Eur J.* 2013;19(44):14823–30. <https://doi.org/10.1002/chem.201302849>
28. Silva VD, Simões TA, Loureiro FJA, Fagg DP, Medeiros ES, Macedo DA. Electrochemical assessment of  $\text{Ca}_3\text{Co}_4\text{O}_9$  nanofibers obtained by solution blow spinning. *Mater Lett.* 2018;221:81–4. <https://doi.org/10.1016/j.matlet.2018.03.088>
29. Bittner M, Helmich L, Nietschke F, Geppert B, Oeckler O, Feldhoff A. Porous  $\text{Ca}_3\text{Co}_4\text{O}_9$  with enhanced thermoelectric properties derived from sol-gel synthesis. *J Eur Ceram Soc.* 2017;37(13):3909–15. <https://doi.org/10.1016/j.jeurceramsoc.2017.04.059>
30. Yang A, Tao X, Pang GKH, Siu KGG. Preparation of porous tin oxide nanobelts using the electrospinning technique. *J Am Ceram Soc.* 2008;91(1):257–62. <https://doi.org/10.1111/j.1551-2916.2007.02106.x>
31. Koombhongse S, Liu W, Reneker D. Flat polymer ribbons and other shapes by electrospinning. *J Polym Sci B: Polym Phys.* 2001;39:2598–606. <https://doi.org/10.1002/polb.10015>
32. He Z, Liu Q, Hou H, Gao F, Tang B, Yang W. Tailored electrospinning of  $\text{WO}_3$  nanobelts as efficient ultraviolet photodetectors with photo-dark current ratios up to 1000. *ACS Appl Mater Interfaces.* 2015;7(20):10878–85. <https://doi.org/10.1021/acsami.5b02020>
33. Valalaki K, Benech P, Galiouna Nassiopoulou A. High Seebeck coefficient of porous silicon: study of the porosity dependence. *Nanoscale Res Lett.* 2016;11(1):201. <https://doi.org/10.1186/s11671-016-1411-z>
34. Lee H, Vashae D, Wang DZ, Dresselhaus MS, Ren ZF, Chen G. Effects of nanoscale porosity on thermoelectric properties of SiGe. *J Appl Phys.* 2010;107(9):094308. <https://doi.org/10.1063/1.3388076>

## SUPPORTING INFORMATION

Additional supporting information can be found online in the Supporting Information section at the end of this article.

**How to cite this article:** Kruppa K, Maor II, Steinbach F, Beilin V, Mann-Lahav M, Wolf M, et al. Electrospun  $\text{Ca}_3\text{Co}_{4-x}\text{O}_{9+\delta}$  nanofibers and nanoribbons: Microstructure and thermoelectric properties. *J Am Ceram Soc.* 2022;1–12. <https://doi.org/10.1111/jace.18842>